Materials Science & Engineering A 860 (2022) 144288

Contents lists available at ScienceDirect

Materials Science & Engineering A

journal homepage: www.elsevier.com/locate/msea

Effect of heat input on nanomechanical properties of wire-arc additive manufactured Al 4047 alloys

Siqi Liu [a], Di Wan [b,**], Ding Peng [c,***], Xu Lu [b], Xiaobo Ren [d], Yuequn Fu [a], Feng Wang [a], Yanjun Li [e], Zhiliang Zhang [a], Jianying He [a,*]

[a] NTNU Nanomechanical Lab, Department of Structural Engineering, Norwegian University of Science and Technology (NTNU), Trondheim, 7491, Norway
[b] Department of Mechanical and Industrial Engineering, Norwegian University of Science and Technology (NTNU), Trondheim, 7491, Norway
[c] Department of Physics, Norwegian University of Science and Technology (NTNU), Trondheim, 7491, Norway
[d] Metal Production and Processing, SINTEF Industry, N-0314, Oslo, Norway
[e] Department of Materials Science and Engineering, Norwegian University of Science and Technology, Trondheim, 7491, Norway

ARTICLE INFO

Keywords:
Heat input
Additive manufacturing
WAAM
Al–Si alloy
Nanoindentation

ABSTRACT

Heat input is one of the most important process parameters during additive manufacturing (AM). It is of great significance to understand the effect of heat input on the microstructure and nanomechanical properties, as well as the underlying mechanisms. Wire-arc additive manufactured (WAAM-ed) Al 4047 alloys under different heat inputs were produced and studied in this work. The as-manufactured Al alloys showed hypoeutectic microstructure that consisted of primary Al (α-Al) dendrite and ultrafine Al–Si eutectic. The effect of heat input on hardness and strain rate sensitivity (SRS) were investigated through nanoindentation. The nanohardness decreased with the increasing heat input, in accordance with the trend of yield strength and microhardness in the previous studies, in which the mechanism was usually explained by the grain growth model and Hall-Petch relationship. This work suggests a distinct mechanism regarding the effect of heat input on nanohardness, which is the enhanced solid solution strengthening produced by lower heat input. In addition, the heat input had little effect on the SRS and activation volume. It is hoped that this study leads to new insights into the understanding of the relation between heat input and nanomechanical properties, and further benefits to improve the targeted mechanical properties and engineering applications of the AM-ed materials.

1. Introduction

Given the sound weldability, superior strength-to-weight ratio, and excellent corrosion resistance, aluminum-silicon (Al–Si) alloy is an important engineering material [1,2]. Additive manufacturing (AM) has been an emerging technique for fabricating Al–Si alloys, owing to its immense design freedom and rapid fabrication speed [3–5]. Cold metal transfer (CMT) under wire and arc additive manufacturing (WAAM) is a method that reduces the process heat input and provides a high deposition rate, and thus its application in manufacturing Al–Si alloys has gained great attention [6,7].

During the manufacturing process in AM, several processing parameters such as travel speed, heat input, interpass temperature, etc., have been found to have great influences on the performance of the AM-ed compounds [8–10]. In other words, the variable processing parameters can account for the tunable and flexible performance in AM. Therefore, it is crucial to comprehend the effect of processing parameters on the microstructure and mechanical properties of AM-ed materials, namely, the intrinsic relationship of processing-microstructure-property. Linear heat input, which is proportional to voltage and current and inversely proportional to travel speed, is usually used as one of the most important thermal-relative processing parameters in AM [11]. Accordingly, the focus of the present work is on the effect of linear heat input on mechanical properties.

In recent years, a few studies have been devoted to investigating the effect of heat input on the microstructure and mechanical properties of AM-ed alloys [8,12–14]. Su et al. reported that the decrease of heat input slowed down the grain growth rate of the AM-ed Al–Mg alloys, and thus

* Corresponding author.
** Corresponding author.
*** Corresponding author.
E-mail addresses: di.wan@ntnu.no (D. Wan), ding.peng@ntnu.no (D. Peng), jianying.he@ntnu.no (J. He).

https://doi.org/10.1016/j.msea.2022.144288
Received 3 June 2022; Received in revised form 23 September 2022; Accepted 3 November 2022
Available online 9 November 2022

the improvement of micro-hardness was attributed to the smaller grain size [12]. Wang et al. demonstrated a quantitative connection among linear heat input, grain size, and yield strength in AM by investigating the impact of linear heat input on the microstructure and the mechanical properties [8]. As for the underlying mechanism regarding the effect of heat input, the majority of prior research explained it by associating the enhancement in strength at lower heat input with the grain growth model and the Hall-Petch relationship [15,16]. Nevertheless, there is limited work that has put the research focus on the nanomechanical behaviors of different phases in the AM-ed Al alloys and exploring the corresponding mechanisms, and a detailed investigation on this issue is highly required.

Nanoindentation is an effective and suitable approach that operates in the nano or sub-micron depth to capture the nanomechanical properties, which can effectively avoid the influences from grain/phase boundaries [17]. Therefore, nanoindentation is a powerful tool to investigate the local mechanical behaviors in AM-ed materials. Among others, strain rate sensitivity (SRS) is an important time-dependent plastic deformation characteristic and is critical to the comprehension of the thermally activated plastic deformation in metallic materials. In recent studies, the deformation behavior of AM-ed Al alloy has been reported to be strain rate sensitive [18]. Furthermore, the Al alloy can be subjected to a large range of strain rates in several applications such as the automobile and aerospace industry. Accordingly, there is an essential need to investigate the alloy's responses to the variable strain rate, which can be quantified by SRS. Therefore, besides the investigation of hardness, the effects of heat input on SRS and activation volume of AM-ed Al alloys are investigated for the first time.

In the present work, by examining three different WAAM-ed samples, the effect of heat input on the nanomechanical properties of Al 4047 alloy was investigated through nanoindentation. Nanohardness and strain rate sensitivity (SRS) of primary Al and Al–Si eutectic in Al 4047 alloy were studied to reveal the plastic deformation behaviors. Furthermore, the underlying mechanism regarding the influence of heat input on the plastic properties of this alloy, namely the process-property relation, was explored and discussed from the nanoscale perspective.

2. Experimental materials and methods

2.1. Sample preparation

The investigated Al 4047 alloys (containing 12 wt% Si) were fabricated by the CMT-WAAM. The sketch map of the deposition wall is shown in Fig. 1(a), containing 16 layers in total. The average height of each layer is about 3.0–3.5 mm, and the length of the wall is 130 mm. There are in total three samples under various linear heat inputs by adjusting the current and voltage while the same settings of other processing parameters, as summarized in Table 1. The heat input was calculated by the following equation [19]:

$$\mathrm{HI} = \frac{\eta \times I \times U}{TS} \quad (1)$$

Table 1
Processing parameters of the Al 4047 samples.

	Sample 1	Sample 2	Sample 3
Current (A)	95	115	127
Voltage (V)	10.5	10.5	11.3
Wire feed speed (m/min)	5.1	5.8	6.5
Input energy (kJ)	17.6	23	27
Travel speed (mm/s)	9	9	9
Welding time (s)	14.7	14.7	14.7
Waiting time (s)	150	150	150
Average interpass temperature (°C)	100	100	100
Heat input (J/mm)	89	107	128

where I is the current, U is the voltage, η is the efficiency (assumed to be 0.8), and TS is the travel speed.

As illustrated in Fig. 1, the samples were cut from the central section of the WAAM-ed component into approximately 2 × 2 × thickness (cm^3) blocks. Despite that the mechanical properties in different locations might be different due to the complex thermal history, the same location in the center of the wall was selected to perform experiments to avoid the impact of mechanical inhomogeneity in AM. The surfaces x-z section were ground by SiC papers up to grit 4000#, followed by diamond polishing with 3 μm particle size. The surfaces were finalized by electropolishing with H_2SO_4-methanol electrolyte at 12 V for 30 s [20].

2.2. Material assessment methods

Scanning electron microscopy (SEM) was used to examine the microstructure of the samples. The SEM (FEI, APREO) was employed with a solid-state backscattered electron (BSE) detector and a 20 kV accelerating voltage. The chemical compositions were investigated by energy-dispersive X-ray spectroscopy (EDS) mapping. To minimize the potential influence of the inhomogeneity, at least 20 spectra showing the contents of elementary compositions were captured. Electron backscattered diffraction (EBSD), where a NORDIF system integrated into a field emission scanning electron microscope (FESEM, Zeiss Ultra 55 Limited Edition), was used to examine the grain sizes and grain morphology. The working distance was controlled at about 25 mm with a tilt angle of 70° between the sample surface and the incident beam. The accelerating voltage was 20 kV at high current mode, and the aperture was 300 μm. Scanning areas of 1.8 × 1.8 mm^2 with 2.5 μm step size were chosen on a random region in the center of the sample surfaces. Microindents were created close to the scanned areas by a Vickers microhardness tester for the positioning purpose in subsequent nanoindentation testing.

A JEOL JEM ARM200F double aberration-corrected ColdFEG transmission electron microscope operating at 200 kV was used to characterize the microstructure of the nanoparticles found in the materials. While the bright-field scanning transmission electron microscopy (BF-STEM) image was acquired using a JEOL BF-STEM detector, the BF-TEM images and the selected area diffraction (SAD) patterns were taken using Ultrascan CCD camera. A Centurio Large angle SDD-EDS equipped on

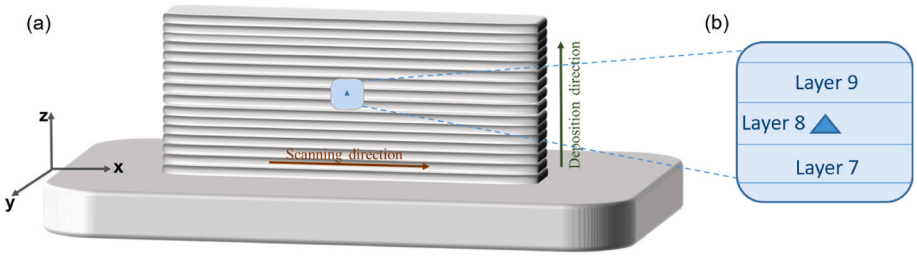

Fig. 1. (a) Sketch map of a typical WAAM deposition wall, showing the location of the cut samples used for microstructure and nanomechanical investigations; (b) sketch map of the cut sample, enlarged from the yellow box in (a), the triangle represents the position of the indentations. (For interpretation of the references to colour in this figure legend, the reader is referred to the Web version of this article.)

the ARM was used for STEM-EDS mapping. The TEM lamella sample was prepared by using the focused ion beam (FIB) FEI Helios G4 UXe DualBeam microscope.

The nanoindentation tests were carried out on the polished surfaces (x-z plane) by using Hysitron Tribo-indenter TI 950 with a Berkovich indenter tip in both standard and multi-range mode. All the measurements were in the same layer (the 8th layer, as shown in Fig. 1(b)) and the inner-layer region among the three samples. The hardness measurements were performed under the load-control mode with the maximum loads of 3 mN and 200 mN, the linear loading and unloading time of 5 s, and the holding time of 2 s at peak loads. The used calculation method for hardness was the recognized Oliver and Pharr (O–P) methods [21,22]. Constant strain rate (CSR) method, with four different strain rates (0.01 s^{-1}, 0.03 s^{-1}, 0.1 s^{-1}, 0.3 s^{-1}), was used to extract the strain rate sensitivity exponent (m). At least 20 indentations were conducted under each condition. For the testing under a maximum load of 3 mN, indentation spacing of 4 μm was utilized to eliminate the possible effects of the overlapping stress fields and plastic deformation zones, and all of the indents fell into the interior of the phase to avoid the influence of the phase boundary.

3. Results

3.1. Microstructure analysis

Al–Si alloys are based on a simple binary eutectic system where the eutectic reaction takes place at 577.6 °C and 12.6 wt% silicon [2,23]. According to the Si content, Al–Si alloys can be divided into hypoeutectic (<11 wt% Si), eutectic (11–13 wt% Si) and hypereutectic (>13 wt% Si) [23].

In order to study the microstructure and grain size distribution in the three samples, EBSD and SEM investigations are carried out. Fig. 2(a)(b)(c) present the EBSD Inverse pole figure (IPF) -Z orientation maps showing the printed microstructure is mainly composed of long columnar dendrite structure with ultrafine secondary dendrite arms and interdendritic eutectics. More detailed structures of the secondary dendrite arms and Al–Si eutectics are shown in the backscatter electron (BSE) images in Fig. 2(d)(e)(f) and Fig. 3. The quantitative information on the grain size is estimated and summarized in Table S1, demonstrating that all the three alloys have average planar grain sizes above 150 μm. Such a large grain size indicates that the dimension of nanoindentation tests is much smaller than the grain size, thus, the nanomechanical properties obtained in the interior of grains and eutectic structure will not be influenced by the grain size and dendrite arm spacing (DAS). As can be seen in Fig. 2, the different heat inputs provide nearly similar microstructure and grain morphology, implying that heat input has little influence on the microstructure.

The representative SEM and TEM characterization results of Sample 1 are presented in Fig. 3, showing the morphology and elemental mapping. The samples investigated in the current work show a typical hypoeutectic microstructure that consists of the primary Al (α-Al) and Al–Si eutectic. Therefore, the microstructure of Al–Si alloys can be influenced by not only the chemical composition of the alloys but also the solidification rate [4]. As can be seen in Fig. 3(a), the dendrites are the α-Al phase, and the region between the dendrites is the Ai-Si eutectic. Fig. 3(b) exhibits a higher magnification image, enlarged from the yellow box in Fig. 3(a), showing the eutectic Si morphology is fibrous. Fig. 3(c) presents the bright-field TEM image that indicates the size of the eutectic silicon is around 200 nm. Such an ultrafine eutectic structure is ascribed to the rapid cooling rate during the AM process [24]. The detailed TEM experiments for investigating nanoscale Si-rich particles found in the Al–Si eutectic region are shown in Fig. S1. Fig. 3 (d)(e)(f) display the energy-dispersive X-ray spectroscopy (EDS) mapping results, demonstrating the distribution of Al and Si elements. The EDS results in the other samples are presented in Fig. S2.

3.2. Hardness measured by nanoindentation

The representative Load-Depth curves under maximum load of 3 mN and 200 mN are exhibited in Fig. 4(a) and (b) respectively. Firstly, the

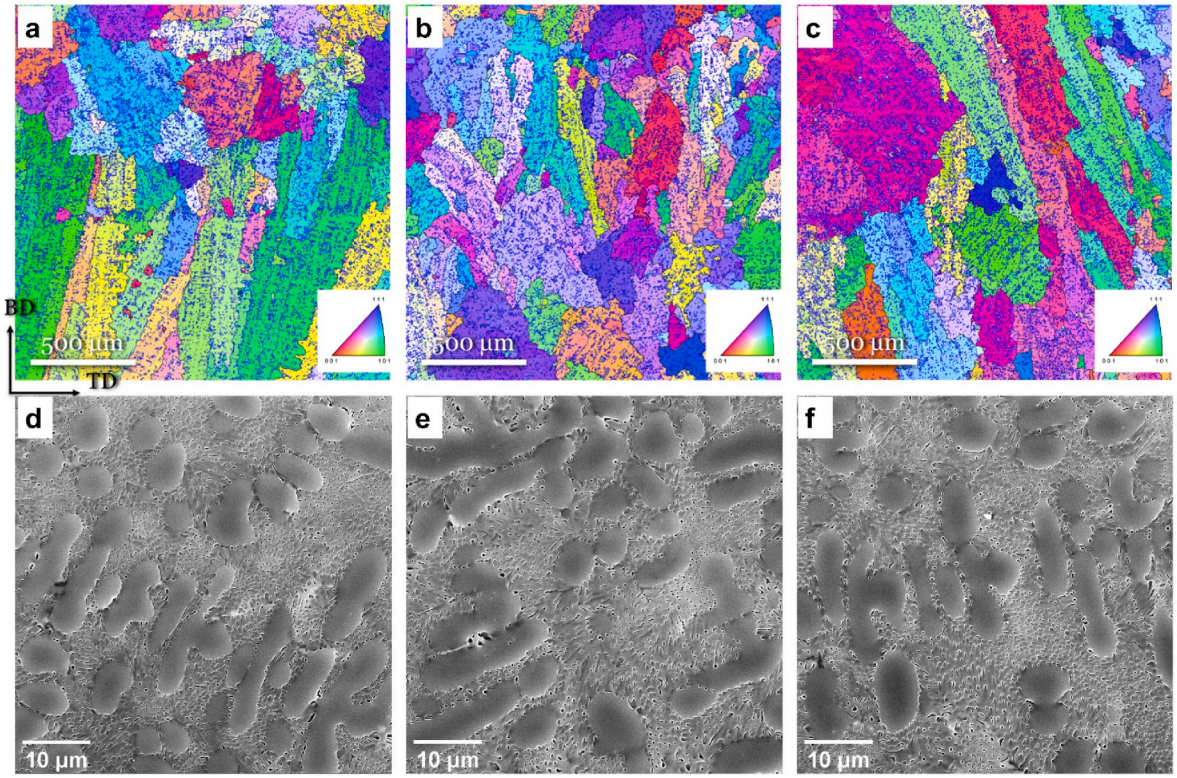

Fig. 2. ND-IPF (IPF-Z) map in (a) Sample 1, (b) Sample 2, (c) Sample 3; SEM image in (d) Sample 1, (e) Sample 2, (f) Sample 3.

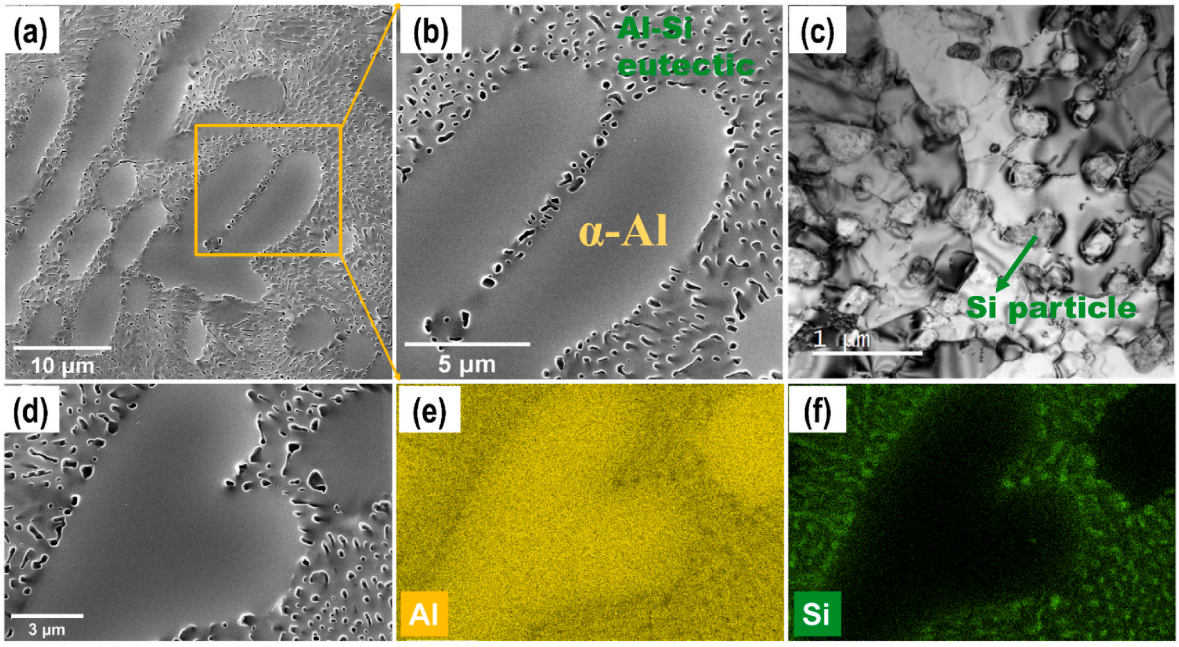

Fig. 3. Representative microstructures of Al 4047 alloy in Sample 1 showing the morphology of primary Al (α-Al) phase and Al–Si eutectic: (a) SEM image; (b) SEM image, enlarged from the yellow box in (a); (c) Bright-field TEM image of Al–Si eutectic region showing the presentation of Si particles embedded in the Al matrix; (d) (e) (f) EDS mapping results, showing the distribution of Al and Si elements. (For interpretation of the references to colour in this figure legend, the reader is referred to the Web version of this article.)

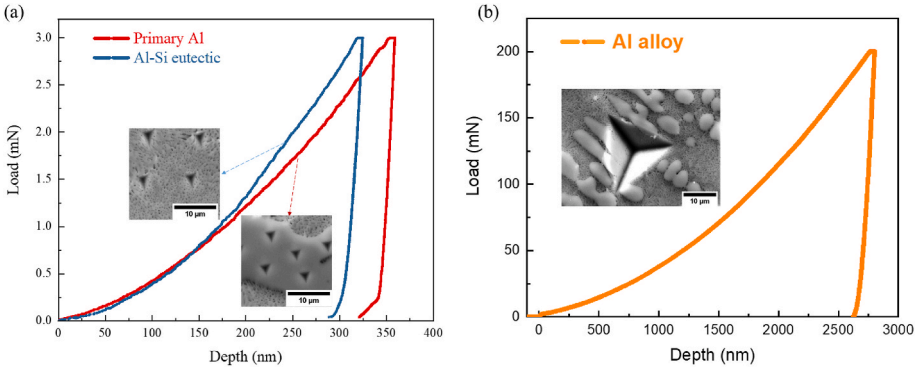

Fig. 4. Representative Load-Displacement curves in Sample 1 of (a) primary Al and eutectic under 3 mN load, and (b) Al alloy under 200 mN. The insets in (a) and (b) are SEM images of indents on the individual structure and integral structure (α-Al dendrite + Al–Si eutectic).

indents under 3 mN are performed on the individual phases in an effort to obtain the local mechanical properties of the α-Al and the Al–Si eutectic, as shown in the SEM images in Fig. 4(a). The displacements of the α-Al phase are larger than that of the Al–Si eutectic, which indicates that the α-Al is softer than the eutectic. Furthermore, as shown in Fig. 4 (b), the indents under 200 mN are large enough to cover a region containing both primary α-Al phase and Al–Si eutectic, which is regarded as representative of the integral property of the Al alloy. At least 30 indents were performed on each sample, in order to minimize the influence of the different volume fractions of α-Al and the Al–Si eutectic.

The effect of heat input on the hardness is investigated both locally and globally. As can be seen in Fig. 5 and Table 2, the hardness values of both α-Al and the eutectic decrease with increasing heat input. Comparing the results of these two components, the hardness of the eutectic is higher than that of the α-Al, owing to the existence of high-density submicron-sized Si particles which have a strong dispersion strengthening effect in the eutectic. For the global value of the Al alloy, as presented in Fig. 5, the hardness decreases with increasing heat input as well, which verifies the impact of heat input on the hardness.

It is interesting to note that the trends shown in this work are consistent with the tendency of the heat input effect on microhardness in the previous studies [8,12]. However, the corresponding mechanism was explained at the microscale in previous studies. It was suggested that larger heat input results in a smaller cooling rate, which is beneficial for grain growth and leads to larger grain size [15]. According to the Hall-Petch relationship, the lower yield strength and hardness arise from the larger grain size [16]. However, the dimension of the performed nanoindentation is far less than the grain size, therefore, the underlying mechanisms interpreted at the microscale are not applicable in this work. The unusual mechanism depicting the effect of heat input exists at the nanoscale, which will be discussed in the next section.

3.3. Strain rate sensitivity and activation volume

Nanoindentation SRS provides a distinct way to capture the intrinsic SRS of a single phase/crystal without the effect of grain size. The representative load-displacement curves at varying indentation strain rates with the applied maximum load of 3 mN and 200 mN are presented

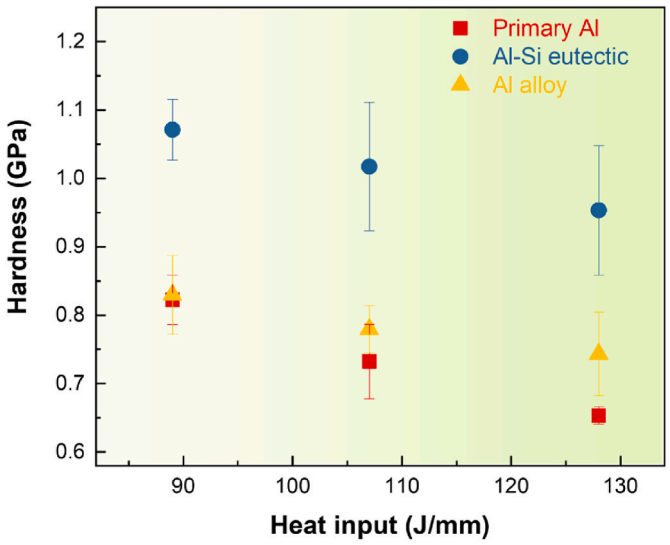

Fig. 5. Effect of heat input on the hardness of individual structures and Al alloy (α-Al dendrite + Al–Si eutectic).

Table 2
The hardness of different microstructural phases with respect to various process parameters.

Heat input (J/mm)		Sample 1	Sample 2	Sample 3
		89	107	128
Hardness(GPa)	Primary Al	0.82 ± 0.036	0.73 ± 0.054	0.65 ± 0.013
	Al–Si eutectic	1.06 ± 0.044	1.02 ± 0.094	0.95 ± 0.095
	Al alloy	0.83 ± 0.057	0.78 ± 0.034	0.74 ± 0.061

in Fig. 6(a) and (b) respectively. As it can be seen, the displacement decreases with increasing strain rate in each case. Substantial pop-in events can be found in the loading curves of the α-Al phase, resulting in the serration increment of displacement, whereas the loading curves of the eutectic do not have obvious pop-in events. It is known that the pop-in events correlate with discrete nucleation of dislocations beneath the indenter [25], Si particles existing in the eutectic structure (see Fig. 3 (c)) may prevent the dislocation nucleation, which may be responsible for the absence of pop-in events in the eutectic.

SRS is a parameter that manifests the dependence of flow stress (σ) on the strain rate ($\dot{\varepsilon}$) at constant strain and temperature, which is an important indicator of the plastic deformation behavior of metallic materials. In uniaxial tension testing, the value of the SRS exponent (m_{uni}) can be determined by the following equation [26]:

$$m_{uni} = \left(\frac{dln(\sigma)}{dln(\dot{\varepsilon})}\right)_{T,\varepsilon} \tag{2}$$

Similarly, the indentation-based SRS exponent can be calculated as defined by Mayo and Nix [27]:

$$m = \frac{dln(H)}{dln(\dot{\varepsilon})} \tag{3}$$

Mayo and Nix approximated that the hardness (H) is independent of the instantaneous indentation depth (h), and thus the indentation strain rate can be estimated as [27,28]:

$$\dot{\varepsilon} = \frac{\dot{h}}{h} = \frac{1}{2}\left(\frac{\dot{P}}{P} - \frac{\dot{H}}{H}\right) \approx \frac{1}{2}\left(\frac{\dot{P}}{P}\right) \tag{4}$$

where $\dot{h}$ is the rate of displacement, $\dot{P}$ is the loading rate, and P is the instantaneous load.

Fig. 7 shows the log-log plots of the hardness versus strain rate and the estimated values of m for the samples. All of the SRS values are positive, which implies that no dynamic strain aging happens during the deformation [18,29]. The effects of the three heat inputs on the SRS are demonstrated in Fig. 7 and Table 3.. The m value has a slight increase with increasing heat input in the α-Al phase, and a slight decrease with increasing heat input is found in the eutectic structure. Nevertheless, this increase and decrease can be considered small or negligible, due to the relatively large deviations of the hardness values in different strain rates. Furthermore, the m value for the Al alloy does not change with the heat input. Accordingly, the m values are independent of the heat input, that is to say, the heat input has little effect on the SRS. On the other side, the values of m for the eutectic structure are found to be much larger than those of the α-Al phase, and the values of the Al alloy are inside the range of the two individual phases.

The apparent activation volume (V), as one interrelated property with SRS, represents the decreasing rate of activation enthalpy with hardness at a certain temperature [30] and can be calculated by:

$$V = 3\sqrt{3}kT\frac{\partial \ln(\dot{\varepsilon})}{\partial(H)} = \frac{3\sqrt{3}kT}{mH} \tag{5}$$

where k is the Boltzmann constant, and T is the absolute temperature in Kelvin. The values of V for the samples are estimated by Eq. (5) and normalized to the cube of Burgers vector (b = 0.286 nm for Al [31]), as summarized in Table 3. Here, the activation volume is associated with the area swept by the dislocations, since dislocations play a dominant role in the plasticity of crystalline materials [32]. The smaller activation volume indicates the easier dislocation nucleation [33].

The estimated activation volume values for all the structures of the samples are summarized in Table 3. The values of activation volume under different heat inputs vary slightly, which can also be considered that there is little influence on the activation volume. Furthermore, the

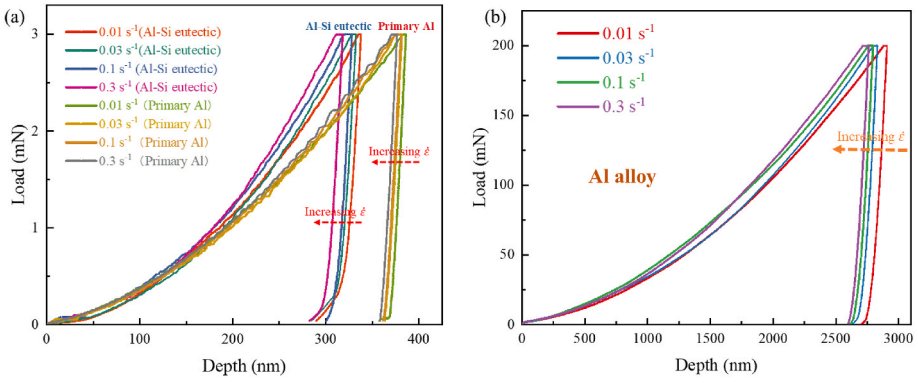

Fig. 6. Representative load-depth curves in Sample 1 with various strain rates under (a) 3 mN, and (b) 200 mN.

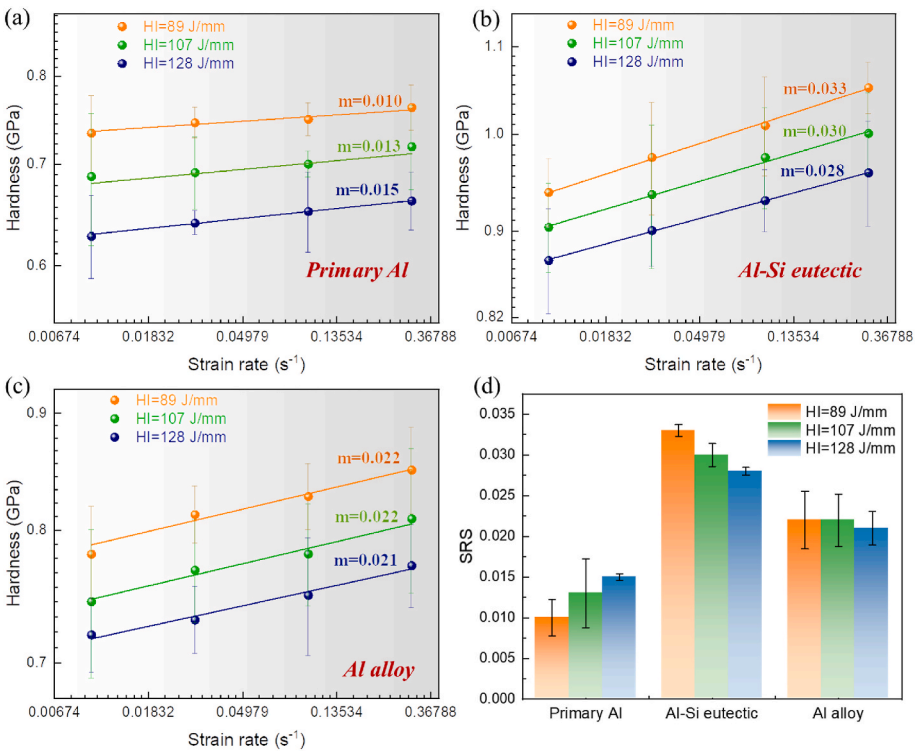

Fig. 7. Logarithmic plots of hardness versus strain rate for determining the values of strain rate sensitivity exponent (m). The effects of heat input on m were shown in the cases of (a) primary Al, (b) eutectic Al–Si, and (c) Al alloy (α-Al dendrite + Al–Si eutectic); (d) the comparison of the SRS values in each condition.

Table 3
Effect of heat input on SRS exponent (m) and activation volume (V).

Heat input (J/mm)		Sample 1	Sample 2	Sample 3
		89	107	128
Strain rate sensitivity exponent/m	Primary Al	0.010	0.013	0.015
	Al–Si eutectic	0.033	0.030	0.028
	Al alloy	0.022	0.022	0.021
Activation volume/V	Primary Al	111.3 b^3	96.2 b^3	93.6 b^3
	Al–Si eutectic	26.1 b^3	29.8 b^3	34.2 b^3
	Al alloy	50.0 b^3	53.2 b^3	57.9 b^3

activation volumes in the Al–Si eutectic are much smaller than those in the α-Al phase. The higher SRS and smaller activation volume can be regarded to delay the development of stress concentrations during plastic deformation [33]. The activation volume of the Al–Si eutectic is around 30 b^3, and it is around 100 b^3 in the α-Al phase. For the Al alloy, the activation volume is around 55 b^3, which is in the range of the values in these two phases. It is noteworthy that SRS and activation volume have been reported to show a clear indentation depth dependence [34,35]. In the current study, the main objective is to compare the SRS under different heat inputs and different phases, and the indentation depth keeps similar for different samples. Typically, for the face-centered cubic (FCC) coarse-grained metallic materials, the deformation mechanism is dislocation intersections cutting through forest dislocation with a large activation volume (~100–1000 b^3) [36,37]. If the internal length scales for dislocation interactions become smaller, e.g. the grain size becomes smaller, the mechanism can be the grain boundary-mediated dislocation process and the activation volume is in the order of atomic volume (~1–10 b^3) [32,38,39]. Consequently, the type of forest–dislocation interaction mechanism can dominate in the α-Al phase. Due to the existence of a large fraction of Al/Si interfaces in the Al–Si eutectic structure, the dislocation interaction at the phase boundary can be the dominant mechanism. A detailed discussion regarding the different deformation mechanisms in these two phases will be given in the next section.

4. Discussion

4.1. Effect of heat input on the nanohardness

It is known that the mechanical properties of Al–Si alloys are closely associated with the size, morphology, and distribution of the eutectic Si phase [40]. Several research efforts have been devoted to the modification of the Si morphology and refinement of the eutectic Si particle [41–45]. The modification of the eutectic structure can be realized by elemental additions, rapid cooling, and heat treatment [43,46,47]. As stated in the results, the rapid cooling in AM process results in the ultrafine eutectic silicon particles (~200 nm), and the difference in the heat input can lead to different cooling rates during AM. However, as shown in Fig. S3, the size and morphology of eutectic Si in the three samples are found to be similar. It should be noted that the nanohardness obtained in the interior of phases will not be influenced by the DAS and the volume of interdendritic Al–Si eutectic and eutectic Si phases, therefore, there are other underlying mechanisms regarding the effect of heat input on nanohardness.

In the primary Al and eutectic Al phase, Si element exist in solid solution, in which solid solution strengthening can be expected. The rapid solidification and high cooling rate during AM process can lead to the solute trapping effect, where the solute concentration is higher than the equilibrium value (solute supersaturation) [40,48]. The higher growth rate of Al dendrites and Al–Si eutectic caused by the higher cooling rate under lower heat input enhances solute trapping of Si elements in the Al phase, and further increases the level of solute supersaturation of Si [49,50]. The silicon contents in the α-Al phase of the three samples were investigated through EDS mapping, and at least 20 spectra showing the contents of elementary compositions were captured

in each condition. As shown in Table 4, the average silicon content in the α-Al phase decreases with the increasing heat input. Consequently, the higher hardness under lower heat input can be attributed to the increased supersaturation of Si in the α-Al and eutectic Al phases, namely, the enhanced solid solution strengthening.

4.2. Strain rate sensitivity and activation volume

The thermally-activated motion of dislocations, such as dislocation interaction, storage, and annihilation, plays a dominant role in the plastic deformation of crystalline metals [26,32]. For understanding the rate dependency of plastic deformation, Orowan's equation, which relates the strain rate to the mobile dislocation density, was proposed and expressed as follows [26,51]:

$$\dot{\varepsilon} = M\rho_m b\bar{v} \tag{6}$$

where M is the reciprocal of Schmidt factor, ρ_m is the mobile dislocation density, and $\bar{v}$ is the average velocity of the mobile dislocation. Therefore, the change in strain rate can result in a changing mobile dislocation density and dislocation velocity that are relevant to the dislocation storage or annihilation.

Recent investigations have demonstrated that the enhanced SRS in ultrafine-grained metals or nanocrystalline materials is attributable to the thermally activated annihilation of dislocations along the grain boundaries [52,53]. A significant difference between the α-Al phase and the Al–Si eutectic structure is the existence of phase interfaces in the latter. The Al–Si interfaces can also act as the dislocation sources and sinks similar to grain boundaries [52,53], which allow easy climb and annihilation of dislocations along the interfaces. Due to the high fraction of interface volume in the Al–Si eutectic phase, dislocations are stored near the phase interfaces, in which the dislocation annihilation occurs during the climbing processes [54]. Therefore, compared to the α-Al phase, the greater change in mobile dislocation density caused by dislocation annihilation along the interfaces in the Al–Si eutectic is responsible for the higher SRS and lower activation volume.

5. Conclusion

In the current work, in order to examine the effect of heat input on the nanomechanical properties of the wire-arc additively manufactured (WAAM-ed) Al 4047 alloy, the nanoindentation technique was employed. Hardness and strain rate sensitivity (SRS) were investigated on different scales. The main conclusion can be summarized as follows:

1. The hardness of both α-Al and eutectic phase decreases with the increasing heat input, which is in agreement with the trend of yield strength and microhardness in the previous studies.
2. The underlying mechanism regarding the effect of heat input on nanohardness was revealed, that is, the enhanced solute strengthening effect plays a dominant role.
3. The heat input was found to have little effect on the SRS and activation volume in both α-Al and Al–Si eutectic phases.
4. Higher SRS and lower activation volume were found in the Al–Si eutectic, which is largely ascribed to the large fraction of Al–Si interfaces, in which the dislocation can easily climb and annihilate.

With these novel insights, this work contributes to a profound understanding of the effect of heat input on the mechanical properties from the nanoscale view.

CRediT authorship contribution statement

Siqi Liu: Conceptualization, Methodology, Investigation, Writing – original draft, Writing – review & editing, Formal analysis, Visualization, Validation. **Di Wan:** Formal analysis, Investigation, Validation, Writing – review & editing. **Ding Peng:** Investigation, Writing – review & editing. **Xu Lu:** Investigation. **Xiaobo Ren:** Resources, Writing – review & editing. **Yuequn Fu:** Writing – review & editing, Formal analysis. **Feng Wang:** Investigation. **Yanjun Li:** Writing – review & editing. **Zhiliang Zhang:** Writing – review & editing, Supervision. **Jianying He:** Validation, Writing – review & editing, Supervision, Funding acquisition.

Table 4
The average silicon content in the α-Al phase of the three samples.

	Sample 1	Sample 2	Sample 3
Heat input (J/mm)	89	107	128
Si content at% in α-Al	2.06 ± 0.17	1.51 ± 0.14	1.27 ± 0.09

Declaration of competing interest

The authors declare that they have no known competing financial interests or personal relationships that could have appeared to influence the work reported in this paper.

Data availability

Data will be made available on request.

Acknowledgments

The Research Council of Norway is acknowledged for the support to the projects (Grant No. 251068; 295864; 237900; 197405). In addition, the Chinese Scholarship Council is acknowledged for the support of this work.

Appendix A. Supplementary data

Supplementary data to this article can be found online at https://doi.org/10.1016/j.msea.2022.144288.

References

[1] N. Kang, P. Coddet, H. Liao, T. Baur, C. Coddet, Wear behavior and microstructure of hypereutectic Al-Si alloys prepared by selective laser melting, Appl. Surf. Sci. 378 (2016) 142–149, https://doi.org/10.1016/j.apsusc.2016.03.221.
[2] G.P. Dinda, A.K. Dasgupta, S. Bhattacharya, H. Natu, B. Dutta, J. Mazumder, Microstructural characterization of laser-deposited Al 4047 alloy, Metall. Mater. Trans. A Phys. Metall. Mater. Sci. 44 (2013) 2233–2242, https://doi.org/10.1007/s11661-012-1560-3.
[3] S. Liu, M. Lin, X. Wang, Y. Fu, X. Ren, Z. Zhang, J. He, A framework for predicting the local stress-strain behaviors of additively manufactured multiphase alloys in the sequential layers, Mater. Sci. Eng. 832 (2022), 142367, https://doi.org/10.1016/j.msea.2021.142367.
[4] D. Herzog, V. Seyda, E. Wycisk, C. Emmelmann, Additive manufacturing of metals, Acta Mater. 117 (2016) 371–392, https://doi.org/10.1016/j.actamat.2016.07.019.
[5] S. Liu, Z. Chang, Y. Fu, Y. Liu, M. Lin, X. Ren, W. Wang, Z. Zhang, J. He, Nanoscale creep behavior and its size dependency of a Zr-based bulk metallic glass manufactured by selective laser melting, SSRN Electron. J. 218 (2022), 110723, https://doi.org/10.2139/ssrn.4014016.
[6] M.M. Tawfik, M.M. Nemat-Alla, M.M. Dewidar, Enhancing the properties of aluminum alloys fabricated using wire + arc additive manufacturing technique - a review, J. Mater. Res. Technol. 13 (2021) 754–768, https://doi.org/10.1016/j.jmrt.2021.04.076.
[7] L. Sun, X. Ren, J. He, Z. Zhang, Numerical investigation of a novel pattern for reducing residual stress in metal additive manufacturing, J. Mater. Sci. Technol. 67 (2021) 11–22, https://doi.org/10.1016/J.JMST.2020.05.080.
[8] Z. Wang, T.A. Palmer, A.M. Beese, Effect of processing parameters on microstructure and tensile properties of austenitic stainless steel 304L made by directed energy deposition additive manufacturing, Acta Mater. 110 (2016) 226–235, https://doi.org/10.1016/j.actamat.2016.03.019.
[9] D. Deng, R.L. Peng, H. Brodin, J. Moverare, Microstructure and mechanical properties of Inconel 718 produced by selective laser melting: sample orientation dependence and effects of post heat treatments, Mater. Sci. Eng. 713 (2018) 294–306, https://doi.org/10.1016/j.msea.2017.12.043.
[10] X.P. Li, M.P. Roberts, S. O'Keeffe, T.B. Sercombe, Selective laser melting of Zr-based bulk metallic glasses: processing, microstructure and mechanical properties, Mater. Des. 112 (2016) 217–226, https://doi.org/10.1016/j.matdes.2016.09.071.

[11] T. DebRoy, H.L. Wei, J.S. Zuback, T. Mukherjee, J.W. Elmer, J.O. Milewski, A. M. Beese, A. Wilson-Heid, A. De, W. Zhang, Additive manufacturing of metallic components – process, structure and properties, Prog. Mater. Sci. 92 (2018) 112–224, https://doi.org/10.1016/j.pmatsci.2017.10.001.
[12] C. Su, X. Chen, C. Gao, Y. Wang, Effect of heat input on microstructure and mechanical properties of Al-Mg alloys fabricated by WAAM, Appl. Surf. Sci. 486 (2019) 431–440, https://doi.org/10.1016/j.apsusc.2019.04.255.
[13] E. Aldalur, F. Veiga, A. Suárez, J. Bilbao, A. Lamikiz, High deposition wire arc additive manufacturing of mild steel: strategies and heat input effect on microstructure and mechanical properties, J. Manuf. Process. 58 (2020) 615–626, https://doi.org/10.1016/j.jmapro.2020.08.060.
[14] C. Li, H. Gu, W. Wang, S. Wang, L. Ren, Z. Wang, Z. Ming, Y. Zhai, Effect of heat input on formability, microstructure, and properties of Al-7Si-0.6Mg alloys deposited by CMT-WAAM process, Appl. Sci. 10 (2020), https://doi.org/10.3390/APP10010070.
[15] N.A. Rosli, M.R. Alkahari, M.F. bin Abdollah, S. Maidin, F.R. Ramli, S.G. Herawan, Review on effect of heat input for wire arc additive manufacturing process, J. Mater. Res. Technol. 11 (2021) 2127–2145, https://doi.org/10.1016/j.jmrt.2021.02.002.
[16] N. Hansen, Hall-petch relation and boundary strengthening, Scripta Mater. 51 (2004) 801–806, https://doi.org/10.1016/j.scriptamat.2004.06.002.
[17] C.A. Schuh, Nanoindentation studies of materials, Mater. Today 9 (2006) 32–40, https://doi.org/10.1016/S1369-7021(06)71495-X.
[18] I. Rosenthal, A. Stern, N. Frage, Strain rate sensitivity and fracture mechanism of AlSi10Mg parts produced by Selective Laser Melting, Mater. Sci. Eng. 682 (2017) 509–517, https://doi.org/10.1016/j.msea.2016.11.070.
[19] Z. Li, C. Liu, T. Xu, L. Ji, D. Wang, J. Lu, S. Ma, H. Fan, Reducing arc heat input and obtaining equiaxed grains by hot-wire method during arc additive manufacturing titanium alloy, Mater. Sci. Eng. 742 (2019) 287–294, https://doi.org/10.1016/J.MSEA.2018.11.022.
[20] B. Dong, X. Cai, S. Lin, X. Li, C. Fan, C. Yang, H. Sun, Wire arc additive manufacturing of Al-Zn-Mg-Cu alloy: microstructures and mechanical properties, Addit. Manuf. 36 (2020), 101447, https://doi.org/10.1016/j.addma.2020.101447.
[21] W.C. Oliver, G.M. Pharr, An improved technique for determining hardness and elastic modulus using load and displacement sensing indentation experiments, J. Mater. Res. 7 (1992) 1564–1583, https://doi.org/10.1557/jmr.1992.1564.
[22] S. Liu, D. Wan, S. Guan, Y. Fu, X. Ren, Z. Zhang, J. He, Microstructure and nanomechanical behavior of an additively manufactured (CrCoNiFe)94Ti2Al4 high-entropy alloy, Mater. Sci. Eng. 823 (2021), 141737, https://doi.org/10.1016/J.MSEA.2021.141737.
[23] G.P. Dinda, A.K. Dasgupta, J. Mazumder, Evolution of microstructure in laser deposited Al-11.28%Si alloy, Surf. Coating. Technol. 206 (2012) 2152–2160, https://doi.org/10.1016/j.surfcoat.2011.09.051.
[24] J. Abboud, J. Mazumder, Developing of nano sized fibrous eutectic silicon in hypereutectic Al–Si alloy by laser remelting, Sci. Rep. 10 (2020) 1–18, https://doi.org/10.1038/s41598-020-69072-1, 2020 101.
[25] J.K. Mason, A.C. Lund, C.A. Schuh, Determining the activation energy and volume for the onset of plasticity during nanoindentation, Phys. Rev. B Condens. Matter 73 (2006) 1–14, https://doi.org/10.1103/PhysRevB.73.054102.
[26] K. Durst, V. Maier, Dynamic nanoindentation testing for studying thermally activated processes from single to nanocrystalline metals, Curr. Opin. Solid State Mater. Sci. 19 (2015) 340–353, https://doi.org/10.1016/j.cossms.2015.02.001.
[27] M.J. Mayo, W.D. Nix, A micro-indentation study of superplasticity in Pb, Sn, and Sn-38 wt% Pb, Acta Metall. 36 (1988) 2183–2192, https://doi.org/10.1016/0001-6160(88)90319-7.
[28] T. Maity, B. Roy, J. Das, Mechanism of lamellae deformation and phase rearrangement in ultrafine β-Ti/FeTi eutectic composites, Acta Mater. 97 (2015) 170–179, https://doi.org/10.1016/j.actamat.2015.07.007.
[29] F. Kabirian, A.S. Khan, A. Pandey, Negative to positive strain rate sensitivity in 5xxx series aluminum alloys: experiment and constitutive modeling, Int. J. Plast. 55 (2014) 232–246, https://doi.org/10.1016/j.ijplas.2013.11.001.
[30] M.J. Soni, S.K. Shekh, Sharma, S.K. Mishra, Strain rate sensitivity behaviour of the thin films of Al, Al[sbnd]Si and nanocomposite Al-Si-N: a comparative study, Mater. Char. 169 (2020), 110589, https://doi.org/10.1016/j.matchar.2020.110589.
[31] B. Bose, R.J. Klassen, Effect of copper addition and heat treatment on the depth dependence of the nanoindentation creep of aluminum at 300 K, Mater. Sci. Eng. 500 (2009) 164–169, https://doi.org/10.1016/j.msea.2008.09.018.
[32] Y. Xiao, V. Maier-Kiener, J. Michler, R. Spolenak, J.M. Wheeler, Deformation behavior of aluminum pillars produced by Xe and Ga focused ion beams: insights from strain rate jump tests, Mater. Des. 181 (2019), 107914, https://doi.org/10.1016/j.matdes.2019.107914.
[33] T. Maity, K.G. Prashanth, Balçi, Z. Wang, Y.D. Jia, J. Eckert, Plastic deformation mechanisms in severely strained eutectic high entropy composites explained via strain rate sensitivity and activation volume, Compos. B Eng. 150 (2018) 7–13, https://doi.org/10.1016/j.compositesb.2018.05.033.
[34] M. Haghshenas, R.J. Klassen, Assessment of the depth dependence of the indentation stress during constant strain rate nanoindentation of 70/30 brass, Mater. Sci. Eng. 572 (2013) 91–97, https://doi.org/10.1016/j.msea.2013.02.009.
[35] M. Haghshenas, A. Khalili, N. Ranganathan, On room-temperature nanoindentation response of an Al–Li–Cu alloy, Mater. Sci. Eng. 676 (2016) 20–27, https://doi.org/10.1016/j.msea.2016.08.091.
[36] A. Dutta, J. Das, Strain rate sensitivity and deformation mechanism of nano-lamellar γ-Ni/Ni 5 Zr eutectic at room temperature, J. Mater. Res. 35 (2020) 2777–2788, https://doi.org/10.1557/jmr.2020.188.
[37] M.A. Meyers, A. Mishra, D.J. Benson, Mechanical properties of nanocrystalline materials, Prog. Mater. Sci. 51 (2006) 427–556, https://doi.org/10.1016/j.pmatsci.2005.08.003.
[38] R. Fritz, D. Wimler, A. Leitner, V. Maier-Kiener, D. Kiener, Dominating deformation mechanisms in ultrafine-grained chromium across length scales and temperatures, Acta Mater. 140 (2017) 176–187, https://doi.org/10.1016/j.actamat.2017.08.043.
[39] M. Haghshenas, V. Bhakhri, R. Oviasuyi, R.J. Klassen, Effect of temperature and strain rate on the mechanisms of indentation deformation of magnesium, MRS Commun. 5 (2015) 513–518, https://doi.org/10.1557/mrc.2015.57.
[40] H.R. Kotadia, G. Gibbons, A. Das, P.D. Howes, A review of laser powder bed fusion additive manufacturing of aluminium alloys: microstructure and properties, Addit. Manuf. 46 (2021), 102155, https://doi.org/10.1016/j.addma.2021.102155.
[41] X.P. Li, X.J. Wang, M. Saunders, A. Suvorova, L.C. Zhang, Y.J. Liu, M.H. Fang, Z. H. Huang, T.B. Sercombe, A selective laser melting and solution heat treatment refined Al-12Si alloy with a controllable ultrafine eutectic microstructure and 25% tensile ductility, Acta Mater. 95 (2015) 74–82, https://doi.org/10.1016/j.actamat.2015.05.017.
[42] S. Hegde, K.N. Prabhu, Modification of eutectic silicon in Al–Si alloys, J. Mater. Sci. 43 (2008) 3009–3027, https://doi.org/10.1007/S10853-008-2505-5, 2008 439.
[43] D. Jiang, J. Yu, Simultaneous refinement and modification of the eutectic Si in hypoeutectic Al–Si alloys achieved via the addition of SiC nanoparticles, J. Mater. Res. Technol. 8 (2019) 2930–2943, https://doi.org/10.1016/J.JMRT.2019.05.001.
[44] Y. Zhang, Y. Guo, Y. Chen, Y. Cao, H. Qi, S. Yang, Microstructure and mechanical properties of Al-12Si alloys fabricated by ultrasonic-assisted laser metal deposition, Materials 13 (2019) 126, https://doi.org/10.3390/ma13010126.
[45] L.Z. Zhao, M.J. Zhao, L.J. Song, J. Mazumder, Ultra-fine Al-Si hypereutectic alloy fabricated by direct metal deposition, Mater. Des. 56 (2014) 542–548, https://doi.org/10.1016/j.matdes.2013.11.059.
[46] H.H. Lien, J. Mazumder, J. Wang, A. Misra, Ultrahigh strength and plasticity in laser rapid solidified Al–Si nanoscale eutectics, Mater. Res. Lett. 8 (2020) 291–298, https://doi.org/10.1080/21663831.2020.1755380.
[47] S. Moniri, A.J. Shahani, Chemical modification of degenerate eutectics: a review of recent advances and current issues, J. Mater. Res. 34 (2019) 20–34, https://doi.org/10.1557/JMR.2018.361.
[48] J.H. Rao, Y. Zhang, K. Zhang, A. Huang, C.H.J. Davies, X. Wu, Multiple precipitation pathways in an Al-7Si-0.6Mg alloy fabricated by selective laser melting, Scripta Mater. 160 (2019) 66–69, https://doi.org/10.1016/J.SCRIPTAMAT.2018.09.045.
[49] J.D. Roehling, D.R. Coughlin, J.W. Gibbs, J.K. Baldwin, J.C.E. Mertens, G. H. Campbell, A.J. Clarke, J.T. McKeown, Rapid solidification growth mode transitions in Al-Si alloys by dynamic transmission electron microscopy, Acta Mater. 131 (2017) 22–30, https://doi.org/10.1016/j.actamat.2017.03.061.
[50] B. Dang, X. Zhang, Y.Z. Chen, C.X. Chen, H.T. Wang, F. Liu, Breaking through the strength-ductility trade-off dilemma in an Al-Si-based casting alloy, Sci. Rep. 6 (2016) 1–10, https://doi.org/10.1038/srep30874.
[51] S.L. Yan, H. Yang, H.W. Li, X. Yao, Variation of strain rate sensitivity of an aluminum alloy in a wide strain rate range: mechanism analysis and modeling, J. Alloys Compd. 688 (2016) 776–786, https://doi.org/10.1016/j.jallcom.2016.07.077.
[52] M. Ruppert, C. Schunk, D. Hausmann, H.W. Höppel, M. Göken, Global and local strain rate sensitivity of bimodal Al-laminates produced by accumulative roll bonding, Acta Mater. 103 (2016) 643–650, https://doi.org/10.1016/j.actamat.2015.11.009.
[53] W. Blum, X.H. Zeng, A simple dislocation model of deformation resistance of ultrafine-grained materials explaining Hall-Petch strengthening and enhanced strain rate sensitivity, Acta Mater. 57 (2009) 1966–1974, https://doi.org/10.1016/j.actamat.2008.12.041.
[54] J. Bach, M. Stoiber, L. Schindler, H.W. Höppel, M. Göken, Deformation mechanisms and strain rate sensitivity of bimodal and ultrafine-grained copper, Acta Mater. 186 (2020) 363–373, https://doi.org/10.1016/j.actamat.2019.12.044.